Non-Newtonian unconfined flow and heat transfer over a heated cylinder using the direct-forcing immersed boundary–thermal lattice Boltzmann method

A. Amiri Delouei,[1,*] M. Nazari,[1,†] M. H. Kayhani,[1,‡] and S. Succi[2,§]
[1]*Mechanical Engineering Department, Shahrood University of Technology, Shahrood, Iran*
[2]*IAC-CNR, Rome, Via dei Taurini 19, 00185, Roma, Italy*
and Physics Department, Harvard University, 60 Oxford Street, Cambridge, Massachusetts 02138, USA
(Received 9 December 2013; revised manuscript received 1 March 2014; published 20 May 2014)

In this study, the immersed boundary–thermal lattice Boltzmann method has been used to simulate non-Newtonian fluid flow over a heated circular cylinder. The direct-forcing algorithm has been employed to couple the off-lattice obstacles and on-lattice fluid nodes. To investigate the effect of boundary sharpness, two different diffuse interface schemes are considered to interpolate the velocity and temperature between the boundary and computational grid points. The lattice Boltzmann equation with split-forcing term is applied to consider the effects of the discrete lattice and the body force to the momentum flux, simultaneously. A method for calculating the Nusselt number based on diffuse interface schemes is developed. The rheological and thermal properties of non-Newtonian fluids are investigated under the different power-law indices and Reynolds numbers. The effect of numerical parameters on the accuracy of the proposed method has been investigated in detail. Results show that the rheological and thermal properties of non-Newtonian fluids in the presence of a heated immersed body can be suitably captured using the immersed boundary thermal lattice Boltzmann method.

DOI: 10.1103/PhysRevE.89.053312 PACS number(s): 47.11.−j

I. INTRODUCTION

Non-Newtonian fluid flow and heat transfer have many practical applications. Multiphase mixtures such as foams, high molecular weight substances (e.g., soap solutions), and polymer melts are some industrial examples of non-Newtonian fluids [1]. The thermal non-Newtonian flow and corresponding hydrodynamic forces over a cylinder play an important role in the formation of weld lines in polymer processing operations [2], and in designing the support structures located in non-Newtonian fluids.

Although the problem of Newtonian fluid flow over a cylinder and its phenomena has been investigated by numerous authors over the years [3–7], the non-Newtonian properties of this problem are much less known with respect to their wide occurrence. Recently, some new types of methods based on the immersed boundary idea of Peskin [8] have been developed that can simplify the solution of complex geometries. The immersed boundary method (IBM) was primarily developed by Peskin [8] to simulate cardiac mechanics and associated blood flow. He indicated that complex flow simulations could be carried out without a body fitted mesh. Nonetheless, in this last decade, the interest in IBMs has grown to a great extent by the introduction of some modifications that overcome most of the original limitations [9,10]. In general, IBM can be defined as a non-body-conformal grid method that satisfies the no-slip boundary condition by implementing a force density (or an energy source density) term to the flow governing equation (or the energy equation). Simplicity, Cartesian frame, reduction of the required amount of memory and CPU time, and simple grid generation process (even for complex geometry) have been introduced in the IBMs as a preferred method with respect to the structured and unstructured body-conformal grid methods. Two general methods exist to evaluate the boundary force density in the IBM. The first method uses the feedback process based on the position (and/or velocity) on the boundary points (feedback-forcing method) [8,11–15] and the second one uses a flow equation to determine the boundary force density (direct-forcing method) [16–19]. The direct-forcing IBM is more common for the assessment of the forcing term [18]. Two important advantages of the direct-forcing algorithm with respect to the feedback algorithm are (i) the forcing term is assessed based on the conventional calculation methods without a stability problem, and (ii) the direct-forcing algorithm does not need arbitrary parameters to be fine-tuned as in the feedback-forcing IBM. The direct-forcing IBM was introduced by Mohd-Yusof [16]. Afterwards, the direct-forcing IBM has been coupled with various numerical frames such as finite-difference [10] or finite-volume method [17]. Given the mismatch between boundary points and computational off-lattice nodes, an interface scheme must be used to couple the boundary and flow field nodes. As for the location of forcing points, the interface schemes can be categorized as *sharp* and *diffuse* interface schemes which the forcing points evaluate in the computational and boundary nodes, respectively. In the diffuse interface scheme, the location of boundary points is traced directly while in the sharp interface scheme, one has to determine the distance of off-lattice points with respect to the boundary curve of the immersed boundary (IB). Because of the simplicity and flexibility of application, the diffuse interface scheme is preferred in the present study. In the diffuse interface scheme, the boundary is considered as a set of the off-lattice forcing points on the boundary, and the flow field is taken as on-lattice computational nodes. The effects of the boundary force must be distributed across the neighboring fluid domain by implementing discrete delta functions. The diffuse interface scheme in the direct-forcing method was first

*a.a.delouei@gmail.com
†Corresponding author: mnazari@shahroodut.ac.ir
‡h_kayhani@shahroodut.ac.ir
§s.succi@iac.cnr.it

introduced by Silva *et al.* [18]. They applied a second-order Lagrange polynomial approximation to calculate the boundary force.

Because of simplicity, computational efficiency, and high accuracy, the lattice Boltzmann method (LBM) has been used to evaluate the velocity of off-lattice flow nodes. Besides, this method takes advantage of a Cartesian frame. Unlike conventional numerical methods that used the Navier-Stokes equation (NSE) based on the macroscopic continuum system, the LBM is a mesoscopic approach based on the kinetic theory of gases [19,20]. With its roots in kinetic theory and high level of scalability on parallel simulation, LBM is getting more and more popular compared with Navier-Stokes equation solvers. The basic concepts of theory of the lattice Boltzmann equation and its application are presented by Benzi *et al.* [21]. The use of the LBM for solving Newtonian flows has increased considerably in recent years [19,20,22,23]. In the case of non-Newtonian flows, the viscosity is not constant which can cause instability in the solution process [24,25]. However, due to the kinetic nature of LBM, it allows straightforward calculations of the local shear rate to second-order accuracy independent of the velocity field [26,27]. Aharonov and Rothman [28] were the first researchers who demonstrated the feasibility of solving the power-law model of non-Newtonian flows using the LBM method. The accuracy of the LBM method for simulating the shear-thinning and shear-thickening power-law fluids has been investigated by Gabbanelli *et al.* [26]. Melchionna *et al.* [29] have presented the ability of the lattice Boltzmann method for the computational study of large-scale cardiovascular blood flow. They exhibit the practicality of their numerical method through a set of large-scale simulations of the flow patterns related to the arterial tree of a patient. They employ 200 000 000 computational cells and compute endothelial shear stress with high accuracy. Nejat *et al.* [30] used the LBM method to investigate the effects of Reynolds number, power-law index, and the distance between the cylinders in the non-Newtonian flows past confined cylinders. Fallah *et al.* [31] used the multiple-relaxation-time method to simulate the non-Newtonian fluid flow over a rotating cylinder. They claim that the local calculation of viscous stresses is one of the advantages of the LBM method for simulating the non-Newtonian fluid flows. Pontrelli *et al.* [32] introduced an unstructured grid lattice Boltzmann method to simulate the non-Newtonian flows in straight and stenosed channels. They affirm that this method can enhance the accuracy of solution by clustering the lattice nodes in the critical regions of the flow. Malaspinas *et al.* [33] have investigated the behavior of a generalized Newtonian fluid by means of a lattice Boltzmann method. They used two non-Newtonian models consisting of power-law and Carreau-law models and show that their second-order accurate method is well suited in complicated geometries. The results of LBM for power-law non-Newtonian fluids have been successfully tested by several researchers [34–36].

There are several LBM simulations of fluid flows in geometries which include curved boundaries [37,38]. Mei *et al.* [37] have presented a second-order boundary treatment of the boundary condition for curved boundaries in the LBM. Also, Guo *et al.* [38] proposed an alternative treatment for curved walls in LBM by decomposing the distribution function at the wall into the equilibrium and the non-equilibrium parts. The LBM method can be utilized for curved boundaries; however, due to uniform Cartesian lattices, the implementation of LBM for curved boundaries requires rather lengthy calculation and procedures. Unlike the modified LBM, in the immersed boundary LBM (IB-LBM), the fluid Cartesian domain is solved by lattice Boltzmann equations, while curved boundaries are treated via a completely separate procedure. The implementation of a curved body in each desired boundary is very simple in the IB-LBM and the extension of this method to thermal cases does not need any extra or new procedure. The application of the immersed boundary method is independent of the specific lattice Boltzmann equation and can be adapted to both single relaxation and multiple-relaxation-time lattice Boltzmann equations (LBEs). In fact, the IB-LBM combines the advantages of both immersed boundary and lattice Boltzmann methods.

In comparison with the works done in the field of non-Newtonian fluids in the presence of IB, the thermal investigation of this problem is rather rare. In fact, the few studies in this area are performed with FLUENT software (finite-volume method) [39–41] or finite-difference method [42]. The immersed boundary–thermal lattice Boltzmann method (IB-TLBM) has been used before for investigating flow [43,44] and heat transfer [45,46] of Newtonian fluids.

For this reason, the direct-forcing immersed boundary–thermal lattice Boltzmann method was used to simulate the non-Newtonian unconfined flows over a heated cylinder. Diffuse interface schemes have been used to distribute the velocity and temperature between the off-lattice obstacle nodes and computational on-lattice nodes. In order to investigate the influence of the sharpness of the boundary on the accuracy of the method, two-point and four-point schemes are used. Developing a simple technique for calculating the Nusselt number in steady and unsteady flows based on the predetermined parameters of direct-forcing IB-TLBM with diffuse interface schemes is another unique aspect of this paper. Our technique is used for investigating Nusselt number and heat transfer from immersed body in shear-thinning and shear-thickening non-Newtonian fluids. The adoption of the structured non-body-conformal grid immersed boundary lattice Boltzmann method relieves the burden of meshing and reduces the amount of memory and CPU time used compared with unstructured body-conformal grids. The power-law non-Newtonian model has been used to investigate the shear-thinning and shear-thickening behaviors of the non-Newtonian flow around the cylinder at different regimes. The split-forcing lattice Boltzmann method proposed by Guo *et al.* [47] has been employed to apply the effect of the immersed body on non-Newtonian flow field. In the LBE with the proposed forcing term, both discrete lattice effect and influences of the body force on the momentum flux are taken into account and the exact Navier-Stokes equations are satisfied [47]. The validation of the employed approach is performed in three cases by considering a non-Newtonian pressure driven flow, the Newtonian flow past an unconfined cylinder in steady and unsteady states, and non-Newtonian fluid flow over a heated cylinder. The effects of the power-law indices and Reynolds numbers on the drag coefficient and recirculation length are studied in steady flows. The drag coefficient, lift coefficient, and Strouhal number in unsteady flows

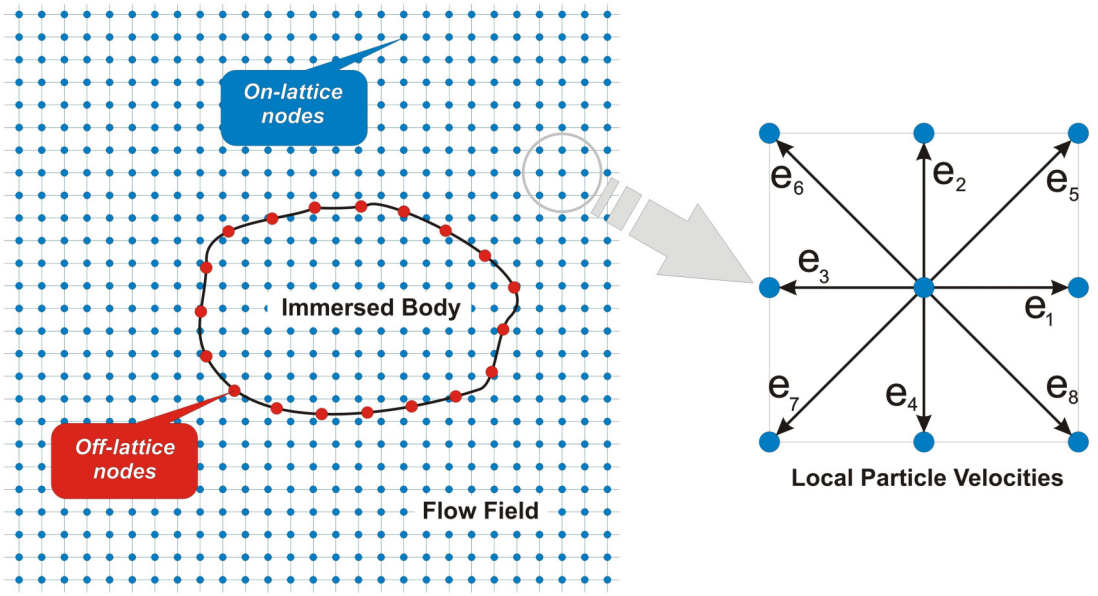

FIG. 1. (Color online) Schematic of an immersed body in the fluid field.

are also studied completely. Also, the effect of shear-thinning and shear-thickening behavior on heat transfer is investigated in both steady and unsteady cases. In addition, the effects of numerical parameters have been investigated in detail. In general, three different states consist of steady flow with no wake; steady flow with axisymmetric wakes and unsteady flow with asymmetric wakes are investigated in the present paper.

II. NON-NEWTONIAN FLUID MODEL

In the Newtonian fluid, the coefficient of viscosity is constant at all rates of shear, whereas the non-Newtonian fluid exhibits a nonlinear relationship between the shear stress and the rate of shear strain, especially at low shear rate. One of the most commonly employed non-Newtonian fluid models for describing the non-Newtonian characteristics of flows is the power-law model. The rheological relationship of the model is as below [48–50]:

$$\mu = m(\dot{\gamma})^{n-1}, \tag{1}$$

where m and n are the consistency index and non-Newtonian behavior index, respectively. m and n are parameters that are determined by curve fitting the equation to physical viscometric data. The viscosity of the fluid increases with the growth of the index m. When $n < 1$, apparent viscosity decreases with the increase of stain rate; the fluid with this character is known as the pseudoplastic or shear-thinning fluid. On the other hand if $n > 1$, apparent viscosity enhances with the increase of stain rate; the fluid with this behavior is called a dilatant or shear-thickening fluid. In the special case which $n = 1$ and $m = \mu_0$, the Newtonian fluid behavior with apparent viscosity of μ_0 will be achieved.

III. NUMERICAL METHODS

In this section, the numerical methods applied for the current study are explained. Here the direct-forcing immersed boundary–thermal lattice Boltzmann method, along with the split-forcing thermal lattice Boltzmann equation (TLBE), is used for the evaluation of boundary force and energy source densities. Also, the interface schemes which are coupled with the numerical method are discussed.

A. Non-Newtonian direct-forcing IB-TLBM based on the split-forcing TLBE

1. Split-forcing lattice Boltzmann method

The lattice Boltzmann equation for the fluid flow (in space $\vec{x}$ and time t) reads as follows (according to the Bhatnagar-Gross-Krook (BGK) model [51]):

$$f_i(\vec{x}+\vec{e}_i\Delta t, t+\Delta t) = f_i(\vec{x},t) - \frac{1}{\tau}\left[f_i(\vec{x},t) - f_i^{(\mathrm{eq})}(\vec{x},t)\right] + F_i(\vec{x},t)\Delta t, \tag{2}$$

where $\vec{e}_i$ is the particle velocity vector in the ith velocity direction of the lattice. Here, we applied the two-dimensional nine-velocity (D2Q9) model so i will be evaluated from zero to 8 (as shown in Fig. 1) [30]. Local particle velocities can be introduced as follows:

$$\vec{e}_i = c\begin{bmatrix} 1 & 0 & -1 & 0 & 1 & -1 & -1 & 1 & 0 \\ 0 & 1 & 0 & -1 & 1 & 1 & -1 & -1 & 0 \end{bmatrix}, \tag{3}$$

where $c = \Delta x/\Delta t$ is the lattice speed and Δx and Δt are the lattice size and the time step size, respectively. $f_i(\vec{x},t)$ and $F_i(\vec{x},t)$ are the particle density distribution and the discrete external force distribution function of the ith direction, respectively. The dimensionless relaxation time of velocity field (τ) expresses the rate at which the local particle distribution relaxes to the local equilibrium state $f_i^{(\mathrm{eq})}(\vec{x},t)$. The equilibrium distribution function, $f_i^{(\mathrm{eq})}(\vec{x},t)$, can be expressed as

$$f_i^{(\mathrm{eq})} = w_i\rho\left[1 + \frac{3}{c^2}(\vec{e}_i\cdot\vec{u}) + \frac{9}{2c^4}(\vec{e}_i\cdot\vec{u})^2 - \frac{3}{2c^2}\vec{u}^2\right], \tag{4}$$

where $w_0 = 4/9$, $w_1 = w_2 = w_3 = w_4 = 1/9$, and $w_5 = w_6 = w_7 = w_8 = 1/36$. The discrete force distribution

function, $F_i(\vec{x},t)$, can be written as

$$F_i(\vec{x},t) = \left(1-\frac{1}{2\tau}\right)w_i\left[3\frac{\vec{e}_i-\vec{u}(\vec{x},t)}{c^2}+9\frac{\vec{e}_i\cdot\vec{u}(\vec{x},t)}{c^4}\vec{e}_i\right]\cdot\vec{F}(\vec{x},t). \tag{5}$$

Based on particle velocity moments of distribution function, the density ρ and the momentum density $\rho\vec{u}$ can be expressed as

$$\rho=\sum_i f_i=\sum_i f_i^{(\mathrm{eq})},\quad \rho\vec{u}=\sum_i \vec{e}_i f_i+\frac{\Delta t}{2}\vec{F}. \tag{6}$$

When a particle moves from point 1 to 2 during one time step, it experiences two different force fields, $F_i(\vec{x}_1,t)$ and $F_i(\vec{x}_2,t+\Delta t)$. In the split-forcing LBE, $F_i(\vec{x}_1,t)$ and $F_i(\vec{x}_2,t+\Delta t)$ are applied during the first and the second half time steps, respectively. In this method, the momentum is affected by the external force on point 2 at time $t+\Delta t$ as well as the force on point 1 at time t [43]. Based on the method of Guo *et al.* [47], the following four steps can be assumed for the split-forcing LBE:

Step 1: First forcing:

$$\rho(\vec{x},t)\vec{u}(\vec{x},t)=\sum_i \vec{e}_i f_i(\vec{x},t)+\frac{\Delta t}{2}\vec{F}(\vec{x},t), \tag{7}$$

Step 2: Collision:

$$f_i'(\vec{x},t)=f_i(\vec{x},t)-\frac{1}{\tau}\left[f_i(\vec{x},t)-f_i^{(\mathrm{eq})}(\vec{x},t)\right], \tag{8}$$

Step 3: Second forcing:

$$f_i''(\vec{x},t)=f_i'(\vec{x},t)+\Delta t\, F_i(\vec{x},t), \tag{9}$$

Step 4: Streaming:

$$f_i(\vec{x}+e_i\,\Delta t,t+\Delta t)=f_i''(\vec{x},t), \tag{10}$$

where f_i' and f_i'' are named post-ollision and postforcing particle distribution functions, respectively [43]. In the lattice Boltzmann method, the consistency between the mesoscopic evolution equation and the macroscopic conservation equations can be regulated by applying the Chapman-Enskog expression [52–55]. The strain rate tensor is macroscopically defined as [54]

$$S_{\alpha\beta}=\tfrac{1}{2}(\nabla_\beta u_\alpha+\nabla_\alpha u_\beta). \tag{11}$$

The strain rate tensor can be obtained locally, too [55]:

$$S_{\alpha\beta}=-\left(1-\frac{1}{\tau}\right)\frac{1}{2\rho\nu}\sum_{i=1}^{9}c_{i\alpha}c_{i\beta}f_i^{(1)}. \tag{12}$$

The pressure can be considered as $p=c_s^2\rho$, so the sound speed, c_s, should be $c_s=1/\sqrt{3}$. Using the first-order Chapman-Enskog expansion of Eq. (12), where $f_i^{(1)}\approx f_i^{(\mathrm{neq})}=f_i-f_i^{(\mathrm{eq})}$, the kinematic viscosity can be achieved as

$$\nu=(2\tau-1)/6. \tag{13}$$

2. *Lattice Boltzmann method for shear-rate-dependent viscosity*

In the shear rate-dependent viscosity fluids, the shear rate, $\dot{\gamma}$, can be calculated from the second invariant of the rate-of-strain tensor as [30]

$$\dot{\gamma}=2\sqrt{D_{ll}}, \tag{14}$$

where

$$D_{ll}=\sum_{\alpha,\beta=1}^{2}S_{\alpha\beta}S_{\alpha\beta}. \tag{15}$$

In order to simulate a shear-dependent non-Newtonian fluid, the shear at each point should be calculated separately. The rate-of-strain tensor can be calculated from the definition of Eq. (11) by implementing the finite-difference method on macroscopic velocities; on the other hand, it is a convenient feature of the lattice Boltzmann method that the rate-of-strain tensor can be achieved locally from Eq. (12) in mesoscopic scale. So, regarding Eq. (14), the local apparent viscosity of a power-law model in each point is

$$\nu(\vec{x},t)=m[2\sqrt{D_{ll}(\vec{x},t)}]^{n-1}. \tag{16}$$

The local apparent relaxation time can be directly calculated from the local apparent viscosity via Eq. (13).

3. *Thermal lattice Boltzmann equation*

The thermal lattice Boltzmann equation with an energy source can be written as [45]

$$g_i(\vec{x}+\vec{e}_i\Delta t,t+\Delta t) = g_i(\vec{x},t)-\frac{1}{\tau_g}\left[g_i(\vec{x},t)-g_i^{(\mathrm{eq})}(\vec{x},t)\right]+Q_i(\vec{x},t)\Delta t, \tag{17}$$

where $g_i(\vec{x},t)$ and $Q_i(\vec{x},t)$ are the energy density distribution functions and discrete energy source functions of the ith direction, respectively. τ_g is the single relaxation time related to the energy equation. The equilibrium internal energy density distribution function, $g_i^{(\mathrm{eq})}(\vec{x},t)$, can introduced as

$$g_i^{(\mathrm{eq})}=\begin{cases}w_i\rho e\left[-1.5\frac{u^2}{c^2}\right], & i=0,\\ w_i\rho e\left[1.5+\frac{1.5}{c^2}(\vec{e}_i\cdot\vec{u})+\frac{9}{2c^4}(\vec{e}_i\cdot\vec{u})^2-\frac{3}{2c^2}\vec{u}^2\right], & i=1,2,3,4,\\ w_i\rho e\left[3+\frac{6}{c^2}(\vec{e}_i\cdot\vec{u})+\frac{9}{2c^4}(\vec{e}_i\cdot\vec{u})^2-\frac{3}{2c^2}\vec{u}^2\right], & i=5,6,7,8.\end{cases} \tag{18}$$

The discrete energy source functions, $Q_i(\vec{x},t)$ can be written as

$$Q_i(\vec{x},t)=\left(1-\frac{1}{2\tau_g}\right)w_i\,Q(\vec{x},t), \tag{19}$$

TABLE I. Explicit diffuse interface scheme's steps (between streaming and collision steps) [43].

(a)	Calculating unforced velocities in Eulerian nodes (u_{ij}^{noF})
(b)	Interpolating the unforced boundary velocities using u_{ij}^{noF}. [$u_b^{noF} = \sum_b u_{ij}^{noF}\, D(x_{ij} - x_b)\, h^2$]
(c)	Evaluating the boundary force on boundary point via Eq. (22) (F_b)
(d)	Distributing the boundary force to neighboring Eulerian nodes. [$F_{ij} = \sum_b F_b\, D(x_{ij} - x_b)\, \Delta s_b$]
(e)	Updating the velocities of neighboring Eulerian nodes.

where Q is the energy source density term. The internal energy per unit mass (e) can be achieved from the following equation:

$$\rho e = \sum_i g_i + \frac{\Delta t}{2}\vec{Q}. \tag{20}$$

Using the Chapman-Enskog expansion, the thermal diffusivity (α) can be achieved as

$$\alpha = \frac{2}{3}\left(\tau_g - \frac{1}{2}\right)c^2\Delta t. \tag{21}$$

Equation (21) will be used for calculating the relaxation times related to TLBE. It is important to mention that similar to split-forcing LBE [Eqs. (7)–(10)], the method of Guo *et al.* [47] is used for applying the energy source density term to the thermal LBE.

4. Direct-forcing method

In this study, the direct-forcing method has been employed to calculate the effects of immersed boundary on fluid flow domain. The desired velocity must satisfy the no-slip condition on the boundary. Considering this fact and the split-forcing LBE which is used for solving the fluid domain, the following direct-forcing relation can be obtained [43]:

$$\vec{F}(\vec{x},t+\Delta t) = 2\rho(\vec{x},t+\Delta t)\frac{\vec{U}^d - \vec{u}^{noF}(\vec{x},t+\Delta t)}{\Delta t}, \tag{22}$$

where U^d and $u^{noF}(\vec{x},t+\Delta t)$ are the desired velocity of the immersed boundary and the unforced velocity at the forcing point, respectively. It is important to mention that the unforced velocity, U^{noF}, can be determined by using the NSE without a forcing term [56,57], or the LBE without a forcing term [58]. Similarly, a direct-forcing formula for the boundary energy-forcing term can be derived [47]:

$$Q(\vec{x},t+\Delta t) = 2\rho(\vec{x},t+\Delta t)\frac{c^2}{3T_0}\frac{T^d - T^{noE}(\vec{x},t+\Delta t)}{\Delta t}, \tag{23}$$

where T^d and $T^{noE}(\vec{x},t+\Delta t)$ are the desired temperature of the immersed boundary and the temperature under no external energy source at $(\vec{x},t+\Delta t)$, respectively.

B. Two-point and four-point diffuse *interface* schemes

In this section, the diffuse interface schemes under the direct-forcing IB-TLBM based on the split-forcing TLBE is introduced. These schemes can be implemented with both explicit and implicit methods. In the diffuse interface scheme, on-lattice computational nodes which extended both inside and outside the immersed boundary have been used for representing the flow field; on the other hand a set of the off-lattice forcing points on the boundary has been used for tracing the presence of IB. In order to evaluate the boundary forces, interpolation from off-lattice boundary nodes and on-lattice neighboring nodes, and vice versa, is needed. Several discrete delta functions were introduced for this purpose [43,52–59]. Here two interpolation methods consisting of a two-point discrete delta function [43] and a four-point discrete delta function [59] are selected as

$$D(\vec{x}_{ij} - \vec{x}_b) = \frac{1}{h^2}d\left(\frac{x_i - x_b}{h}\right)d\left(\frac{y_i - y_b}{h}\right). \tag{24}$$

D represents the discrete delta function and $h = \Delta x$. Related to two-point and four-point discrete delta functions, the shape function d can be achieved from Eqs. (25a) or (25b), respectively.

$$d(r) = \begin{cases} 1 - |r|, & |r| \leqslant 1, \\ 0, & |r| > 1, \end{cases} \tag{25a}$$

or

$$d(r) = \begin{cases} \frac{1}{8}(3 - 2|r| + \sqrt{1 + 4|r| - 4r^2}), & 0 \leqslant |r| < 1, \\ \frac{1}{8}(5 - 2|r| - \sqrt{-7 + 12|r| - 4r^2}), & 1 \leqslant |r| < 2, \\ 0, & |r| \geqslant 2. \end{cases} \tag{25b}$$

Using these two types of discrete delta functions, the effects of the sharpness of the boundary on the solution can be investigated. In the case of a stationary body, the surface force can be calculated as below [14]:

$$\vec{F}_s = -\sum_b \vec{F}(\vec{x}_b)\Delta s_b = -\sum_{i,j}\vec{F}(\vec{x}_{ij})h^2, \tag{26}$$

where Δs_b is the arc length of the boundary segment. There is no difference between the results of the first and second summation.

1. Explicit diffuse interface scheme

In the explicit diffuse interface scheme, the boundary force density (as well as the energy source density) is explicitly obtained. Table I shows the required steps for the explicit diffuse interface scheme. In addition, the schematic of steps (c) and (d) of Table I are depicted in Fig. 2. The small blue points show the on-lattice nodes and bigger red nodes indicate the off-lattice nodes. As shown in Fig. 2, only the limited numbers of on-lattice nodes are affected by specific boundary points. Nonetheless, it should be stressed that when the force density

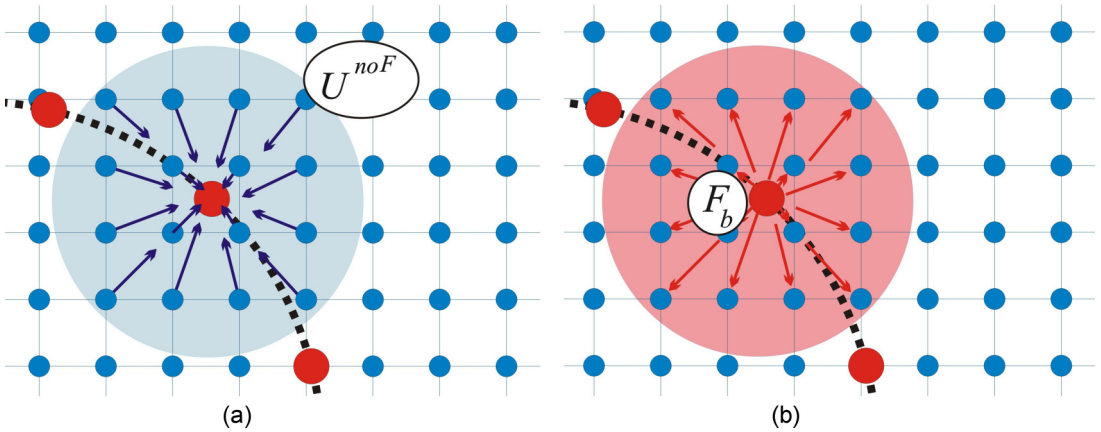

FIG. 2. (Color online) Schematic of velocity and force density exchanges: (a) The unforced velocities interpolated from on-lattice nodes into off-lattice nodes and (b) the force densities distributed from boundary points into flow nodes.

is calculated explicitly, the no-slip boundary condition cannot be guaranteed. There is a similar problem for the evaluation of boundary temperature.

2. *Implicit diffuse interface scheme*

As explained in Table I, the velocity field will be reconstructed by the boundary forces in step (e) of the explicit diffuse interface scheme. However, this forced velocity field may not satisfy the no-slip condition on boundary points because the forces used for forcing the velocities [step (e) in Table I] were extracted from unforced velocities before the update [step (c) in Table I]. To overcome this defect, several implicit forcing methods have been introduced [60–63] which included the complicated matrix calculation in some cases. Here to address the present problem, the multi-direct-forcing method [60,62] is used. Table II shows steps of this method briefly. According to Table II, steps (a)–(e) are similar to the previous section. After these steps, the velocities of the boundary points are interpolated again with the updated neighboring nodes in the flow field. The no-slip boundary condition is checked and steps (c)–(f) are repeated until the desired accuracy is reached. The number of these iterations (NF) determines the degree of implicitness of the multi-direct-forcing method. In the case that there is no iteration, i.e., NF = 1, the previously mentioned explicit forcing interface scheme will be obtained. It is important to mention that similar processes can be applied for calculating the temperature and discrete energy density function between the off-lattice and on-lattice nodes.

C. Nusselt number evaluation

In a heat transfer problem at a surface (boundary) in touch with a fluid, the Nusselt number is defined as the ratio of convective to conductive heat transfer across (normal to) the boundary. Convection includes both advection and diffusion. Here, a simple technique has been developed for calculating the Nusselt number in the direct-forcing immersed boundary–thermal lattice Boltzmann method inspired by the scheme of Wu *et al.* [46]. The Nusselt number on the surface of boundary $(\vec{x}_b,t)$ is introduced as

$$\mathrm{Nu}(\vec{x}_b,t) = \frac{h(\vec{x}_b,t)L_c}{k}, \tag{27}$$

where L_c is characteristic length, h is convective heat transfer coefficient of the fluid, k is thermal conductivity of the fluid, and we have $k = \alpha\,\rho\,c_p$. The heat convection from the immersed boundary should be the same as heat conduction from the immersed boundary. Regarding the Fourier's law and the Newtonian cooling law,

$$h(\vec{x}_b,t)(T_b - T_\infty) = -k\frac{\partial T}{\partial n}(\vec{x}_b,t) = Q(\vec{x}_b,t), \tag{28}$$

where n is the normal direction to the boundary curve in a certain point of the boundary. T_b and T_∞ are the temperature of boundary point and free stream, respectively. The heat flux on the IB $[Q(\vec{x}_b,t)]$ is calculated by Eq. (23), previously. Comparing Eqs. (27) and (28) leads to

$$\mathrm{Nu}(\vec{x}_b,t) = \frac{3T_0L_c}{\alpha\rho c^2(T_b - T_\infty)}Q(\vec{x}_b,t). \tag{29}$$

TABLE II. Implicit diffuse interface scheme's steps (between streaming and collision steps) [43].

(a)	Calculating unforced velocities in Eulerian nodes (u_{ij}^{noF})
(b)	Interpolating the unforced boundary velocities using u_{ij}^{noF}. $[u_b^{noF} = \sum_b u_{ij}^{noF}\,D(x_{ij} - x_b)\,h^2]$
(c)	Evaluating the boundary force on boundary point via Eq. (22) (F_b)
(d)	Distributing the boundary force to neighboring Eulerian nodes. $[F_{ij} = \sum_b F_b\,D(x_{ij} - x_b)\,\Delta s_b]$
(e)	Updating the velocities of neighboring Eulerian nodes (u_{ij}^{F})
(f)	Interpolating the unforced boundary velocities using u_{ij}^{F}. $[u_b^{F} = \sum_b u_{ij}^{F}\,D(x_{ij} - x_b)\,h^2]$
(g)	Iterating steps (c)–(f) until the desired criterion is satisfied.

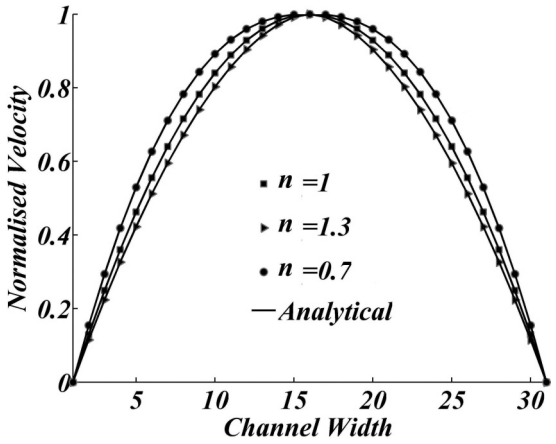

FIG. 3. Non-Newtonian velocity profile for different non-Newtonian power-law indices in the pressure driven channel flow.

The mean Nusselt number over the all IB surface can be obtained by averaging over the entire IB:

$$\overline{\mathrm{Nu}} = \frac{3T_0L_c}{\alpha\rho c^2(T_b - T_\infty)L}\sum_l Q^l(\vec{x}_b,t)\Delta s_b. \qquad (30)$$

So, regarding Eqs. (29) and (30), the Nusselt number of direct-forcing IB-TLBM can be obtained easily by previously determined heat flux at the surface of the IB. Utilizing this technique is simple and time saving because the difficult normal temperature gradient on the IB surface is eliminated.

IV. VALIDATION

The present numerical simulation has been validated thoroughly by analyzing the present results for three test cases: first, a pressure driven flow of power-law fluid inside a channel (see Fig. 3); second, the steady and unsteady flow of Newtonian fluid past a circular cylinder (Table III); and third, the thermal Newtonian flow over a heated cylinder (Table IV).

A. Non-Newtonian channel flow

Since the analytical solution of the two-dimensional velocity profile of a power-law fluid inside a channel is available, this analytical solution is used to validate the non-Newtonian simulation of the presented method. The analytical solution for the velocity parallel to the axis of the channel is as follows [64]:

$$u(y) = \left(\frac{n}{n+1}\right)\left(\frac{G}{m}\right)\left[|H|^{\frac{n+1}{n}} - (H-y)^{\frac{n+1}{n}}\right], \qquad (31)$$

where G represents the constant pressure gradient in the x direction and H is the width of the channel. In Fig. 3, the normalized velocity profile based on the analytical solution [introduced by Eq. (31)] and the velocity profile which was calculated by the present non-Newtonian IB-LBM are shown. Constant velocity and periodic boundary conditions were implemented at the inlet and outlet of the channel, respectively. The no-slip velocities were applied on the two parallel plates. The computational domain consists of 31×101 uniform D2Q9 lattices. The solid walls of the channel are considered as no-slip boundaries of fluid which are treated similarly to the other standard lattice Boltzmann method. Figure 3 has been depicted for three test cases of shear-thinning ($n = 0.7$), Newtonian ($n = 1$), and shear-thickening ($n = 1.3$) flows. The analytical and numerical velocities are in excellent agreement for all test cases.

B. Newtonian steady and unsteady unconfined flow over a circular cylinder

The problem of Newtonian flow over a circular cylinder has been thoroughly investigated by the authors [17,43,44,63,65]. In order to validate the immersed body procedure of the current simulation, the results of the previous published studies for drag coefficient C_D, and recirculation length L_W, in steady state flow are presented in Table III. The recirculation length is calculated by inspecting the stream functions behind the cylinder. Also, the average drag coefficient $\bar{C}_D$, lift coefficient C_L, and Strouhal number St in unsteady state flow are presented in Table III. For the inlet boundary, the Dirichlet boundary condition is used and for the outlet boundary, the homogeneous Neumann boundary condition is used. Regarding the unconfined flow over the cylinder, the free-slip boundary condition is adopted for the far-field boundaries. The same conditions are used in Secs. IV C and V. In this study, the following definition has been used for calculating the drag coefficient, lift coefficient, and Strouhal

TABLE III. Comparison with the previous studies of Newtonian steady and unsteady unconfined flow over a circular cylinder.

		Steady				Unsteady		
		Re = 20		Re = 40		Re = 100		
The characteristics of method	Year	C_D	L_W	C_D	L_W	$\bar{C}_D$	$\pm C_L$	St
Body-fitted grid, NSE, [65]	1998	2.01	–	1	–	1.33	0.33	0.165
Exterior sharp direct-forcing, NSE, [17]	2001	–	–	1.51	–	1.33	0.32	0.165
Implicit diffuse direct-forcing, NSE, [63]	2008	2.07	0.8	1.58	2.49	1.39	0.346	0.16
Implicit diffuse direct-forcing, LBE, [44]	2009	2.091	0.93	1.565	2.31	1.364	0.344	0.163
Exterior sharp direct forcing, LBE, [43]	2009	2.057	0.91	1.538	2.25	1.336	0.329	0.165
Explicit diffuse direct-forcing (two points), LBE	Present	2.061	0.955	1.584	2.342	1.359	0.322	0.163
Explicit diffuse direct-forcing (four points), LBE	Present	2.074	0.974	1.605	2.381	1.370	0.332	0.163
Implicit diffuse direct-forcing (two points), LBE	Present	2.060	0.971	1.591	2.345	1.354	0.321	0.162
Implicit diffuse direct-forcing (four points), LBE	Present	2.072	0.987	1.600	2.382	1.369	0.332	0.163

TABLE IV. Comparison with the previous studies of non-Newtonian unconfined thermal flow over a heated circular cylinder at Re = 40 and Pr = 1.

The characteristics of method	Year	Average of Nusselt number		
		$n = 0.6$	$n = 1.0$	$n = 1.4$
Finite-difference method, NSE [42]	2005	–	3.569	3.3249
Finite-volume method, NSE [41]	2007	–	3.703	3.3522
FLUENT, NSE [40]	2008	4.0545	3.653	3.4003
FLUENT, NSE [39]	2010	4.0775	3.675	3.4216
Implicit diffuse direct-forcing (two points), LBE	Present	4.0518	3.711	3.4671
Implicit diffuse direct-forcing (four points), LBE	Present	4.0636	3.709	3.4614

number:

$$C_D = \frac{F_D}{U_\infty^2 D/2}, \tag{32a}$$

$$C_L = \frac{F_L}{U_\infty^2 D/2}, \tag{32b}$$

$$\mathrm{St} = \frac{f_q D}{U_\infty}, \tag{32c}$$

where drag force, F_D, and lift force, F_L, can be achieved by using Eq. (26). f_q and D are shedding frequency and diameter of the cylinder, respectively. Here the evolutions of lift coefficients are used to calculate the shedding frequency. The comparison between the present numerical data and the values reported in Table III shows that the current IB-LBM simulation has acceptable results. In this study, the computational domain is 40D × 40D with 1601 × 1601 uniform D_2Q_9 lattices.

C. Non-Newtonian unconfined flow over a heated circular cylinder

In order to validate the equations utilized for thermal simulation of the current solution, the average Nusselt number related to the heat transfer over the immersed cylinder is compared. In this section, the method introduced in Sec. III C is used for calculating the Nusselt number. As seen from Table IV, an acceptable agreement between the current split-forcing IB-TLBM and the prior methods presented in Table IV is observed for Newtonian and non-Newtonian fluids.

V. RESULTS AND DISCUSSION

In this section, the introduced direct-forcing IB-TLBM is used to investigate the fluid flow over a circular cylinder. The computational domain is taken as 40D × 40D with 1601 × 1601 uniform grid points. The circular cylinder is considered at the center of the computational domain. The boundary forcing points are uniformly distributed on the cylinder boundary with a spacing of $\Delta s_b = h/1.5$. The following Reynolds number and Prandtl number for a power-law-based flow can be defined:

$$\mathrm{Re}_{pl} = \frac{U_\infty^{(2-n)} D^n}{m}, \tag{33}$$

$$\mathrm{Pr}_{pl} = \frac{m\rho c_p}{k}\left(\frac{U_\infty}{D}\right)^{(n-1)}, \tag{34}$$

where U_∞ represents the free stream velocity. In the next sections, the effects of numerical parameters and flow characteristics are investigated separately.

A. Check the numerical parameters

1. Number of forcing (Re = 10)

In order to find the accuracy of the method in satisfying the no-slip boundary condition on immersed boundary, the following "boundary error" is defined:

$$\text{Boundary error} = \sqrt{\frac{1}{N_{ij}}\sum_i\sum_j\left[\vec{u}_b^{\,n}(i,j) - \vec{u}_b^{\,e}(i,j)\right]^2}, \tag{35}$$

where the superscript e and n refer to the exact and the numerical solution, respectively. In the case of a stationary body, the exact velocity on the boundary (off-lattice nodes) ($\vec{u}_b^{\,e}$) is equal to zero. The values of the numerical value of velocity ($\vec{u}_b^{\,n}$) can be easily determined by step (f) in Table II. N_{ij} is the number of boundary points. The effect of forcing number (NF) on drag coefficient (C_D) and

TABLE V. The effect of number of forcing loops (NF) on drag coefficient and boundary error at Re = 10 at different power-law indices using both the two-point and four-point discrete delta function.

Number of forcing loops	NF = 1	NF = 10	NF = 20	
$n = 0.7$	$\frac{(C_D)_{2p}}{(C_D)_{4p}}$	$\frac{2.936}{2.779}$	$\frac{2.940}{2.800}$	$\frac{2.942}{2.779}$
	$\frac{(B\_\mathrm{Error})_{2p}}{(B\_\mathrm{Error})_{4p}}$	$\frac{2.721\times10^{-3}}{5.198\times10^{-3}}$	$\frac{4.743\times10^{-4}}{7.720\times10^{-5}}$	$\frac{3.358\times10^{-4}}{7.270\times10^{-5}}$
$n = 1.0$	$\frac{(C_D)_{2p}}{(C_D)_{4p}}$	$\frac{2.838}{2.854}$	$\frac{2.841}{2.857}$	$\frac{2.845}{2.858}$
	$\frac{(B\_\mathrm{Error})_{2p}}{(B\_\mathrm{Error})_{4p}}$	$\frac{2.562\times10^{-3}}{5.349\times10^{-3}}$	$\frac{3.596\times10^{-4}}{5.937\times10^{-5}}$	$\frac{2.854\times10^{-4}}{5.501\times10^{-5}}$
$n = 1.3$	$\frac{(C_D)_{2p}}{(C_D)_{4p}}$	$\frac{2.984}{3.079}$	$\frac{2.963}{3.096}$	$\frac{2.871}{3.099}$
	$\frac{(B\_\mathrm{Error})_{2p}}{(B\_\mathrm{Error})_{4p}}$	$\frac{3.051\times10^{-3}}{5.990\times10^{-3}}$	$\frac{3.583\times10^{-4}}{5.816\times10^{-5}}$	$\frac{2.601\times10^{-4}}{4.543\times10^{-5}}$

TABLE VI. The effect of on-lattice grid size on the drag coefficient and boundary error in steady (Re = 10) and unsteady (Re = 100) states and different non-Newtonian power-law indices.

		Re = 10		Re = 100	
		C_D	B_Error	Avg. C_D	B_Error
801 × 801	$n = 0.7$	2.901	4.032×10^{-4}	1.358	5.633×10^{-4}
	$n = 1.0$	2.975	3.327×10^{-4}	1.421	4.835×10^{-4}
	$n = 1.3$	2.894	2.872×10^{-4}	1.523	4.139×10^{-4}
1201 × 1201	$n = 0.7$	3.053	3.889×10^{-4}	1.320	4.167×10^{-4}
	$n = 1.0$	2.954	3.245×10^{-4}	1.372	3.695×10^{-4}
	$n = 1.3$	2.886	2.807×10^{-4}	1.492	3.381×10^{-4}
1601 × 1601	$n = 0.7$	2.942	3.358×10^{-4}	1.307	3.762×10^{-4}
	$n = 1.0$	2.846	2.854×10^{-4}	1.355	3.328×10^{-4}
	$n = 1.3$	2.871	2.601×10^{-4}	1.482	2.949×10^{-4}

boundary-error (BE) at Re = 10 in the Newtonian ($n = 1$), shear-thinning ($n = 0.7$), and shear-thickening ($n = 1.3$) fluids is presented in Table V. The obtained results are provided for both two-point and four-point interface schemes. According to Table II, in the case of NF = 1, only one transition step between the off-lattice and on-lattice nodes takes place and consequently the explicit diffuse interface scheme (as presented in Table I) will result. In Table IV, a significant decrease in the boundary error is seen by increasing the forcing loop number for both two-point and four-point interface schemes.

2. *The effect of on-lattice grid refinement*

In Table VI, the effect of on-lattice grid size on the drag coefficient and boundary error in steady (Re = 10) and unsteady (Re = 100) states for the different non-Newtonian power-law indices is presented. This table is presented for a two-point interface scheme. As the number of computational nodes increases, the boundary error reduces significantly for all cases. The dominant behavior is slow reduction of drag coefficient with respect to the growth of the number of grid points but these variations are different for various Reynolds numbers and power-law indices.

3. *Arc spacing of off-lattice distance (Re = 10)*

Table VII shows the effects of arc spacing of off-lattice distance located on the boundary of IB for different values of power-law indices. According to Table VII, decreasing of Δs_b has no significant effect on the obtained results. Actually, refinement of off-lattice points only increases the speed of convergence. For example, in the case of Newtonian flow (with NF = 20 and using the two-point interface scheme), changing the arc spacing of off-lattice distance from $\Delta s_b = h$ to $\Delta s_b = h/2$ leads to 2.72% reduction in convergence steps.

B. Flow characteristics

1. *Streamlines of different flow regimes*

Figures 4–6 show the streamlines of the non-Newtonian fluid flow over a cylinder for the shear-thinning non-Newtonian ($n = 0.7$), Newtonian, and shear-thickening non-Newtonian ($n = 1.3$) fluid flow, respectively. These figures are associated with different Reynolds numbers using the two-point interface scheme. As shown in this figure, the non-Newtonian fluids with different Reynolds numbers experience different states, i.e., steady flow with no wakes behind the cylinder [Figs. 4(a), 5(a), and 6(a)], steady flow with two axisymmetric wakes [Figs. 4(b), 5(b), and 6(b)], and unsteady shedding flow with two asymmetric wakes [Figs. 4(c), 5(c), and 6(c)]. These different contours show that the flow regime is sensitive to the Reynolds number and power-law index of non-Newtonian fluid. On the other hand, the present results show the ability of the current method for detecting the different states of non-Newtonian fluids.

Figures 4(b), 5(b), and 6(b) show the dependence of the wake length on the power-law index. The recirculation length in Figs. 4(b), 5(b), and 6(b) are 1.945, 2.336, and 2.874, respectively. The wake tends to be shorter in shear-thinning fluids than in Newtonian and shear-thickening fluids at the same value of the Reynolds number. The maximum rate of fluid deformation takes place near the surface; therefore the viscosity is minimum in this region for shear-thinning fluids and a thin layer of low viscosity fluid encapsulates the cylinder. A reduction in the shear rate is observed away from the

TABLE VII. The effects of arc spacing of off-lattice distance (Δs_b) located on the boundary of IB.

Arc spacing of curve boundary distance		$\Delta s_b = h$	$\Delta s_b = h/1.5$	$\Delta s_b = h/2$
$n = 0.7$	C_D	2.943	2.943	2.942
	B_Error	7.556×10^{-5}	3.358×10^{-4}	3.953×10^{-4}
$n = 1.0$	C_D	2.846	2.846	2.843
	B_Error	6.424×10^{-5}	2.854×10^{-4}	3.35×10^{-4}
$n = 1.3$	C_D	2.967	2.884	2.884
	B_Error	6.284×10^{-5}	2.601×10^{-4}	3.109×10^{-4}

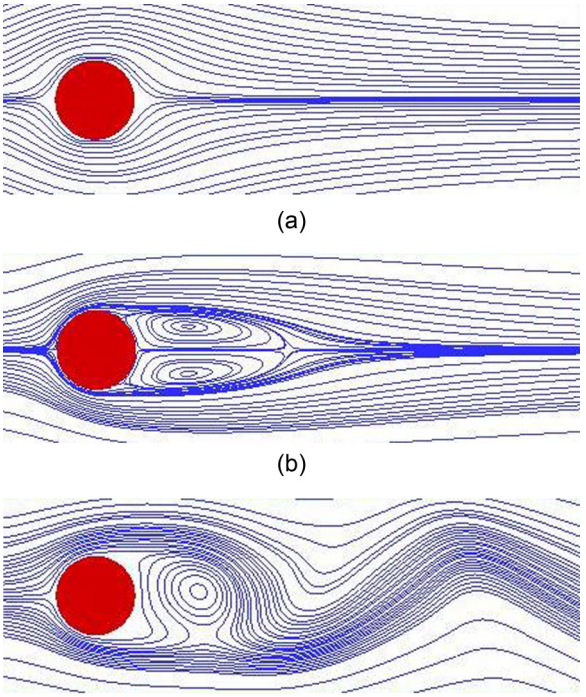

FIG. 4. (Color online) Streamline contours for the shear-thinning non-Newtonian fluid flow ($n = 0.7$) at (a) Re = 1, (b) Re = 40, and (c) Re = 100.

cylinder (yielding high viscosity of the fluid). The latter acts as an effective solid boundary which suppresses the tendency for flow separation, and thus separation is somewhat delayed in shear-thinning fluids. The high shear rate in the vicinity

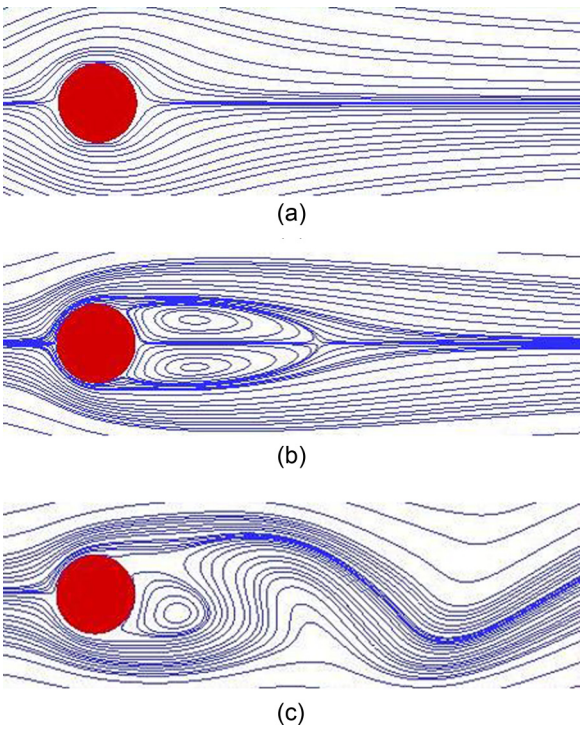

FIG. 5. (Color online) Streamline contours for the Newtonian fluid flow at (a) Re = 1, (b) Re = 40, and (c) Re = 100.

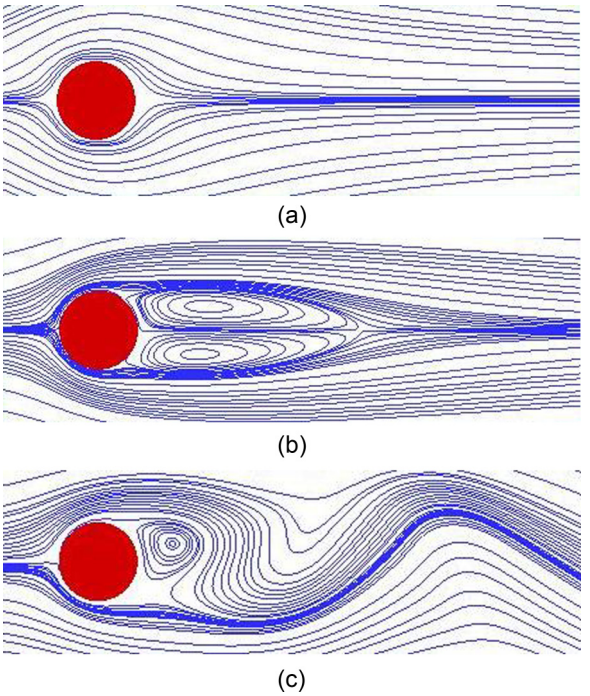

FIG. 6. (Color online) Streamline contours for the shear-thickening non-Newtonian fluid flow ($n = 1.3$) at (a) Re = 1, (b) Re = 40, and (c) Re = 100.

of the cylinder leads to high viscosity for shear-thickening fluids near the surface, and the slow moving viscous fluid encapsulates the cylinder. This slow moving viscous fluid meets the low viscosity fluids away from the cylinder. In other words, for $n > 1$, the maximum viscosity occurs near the surface of the cylinder which progressively decreases elsewhere and therefore, in this case, the effective size of the bluff body increases which will translate into a higher value of the Reynolds number than its nominal value. This leads to an early flow separation in this case. For Newtonian fluids, wake length shows linear dependence on the Reynolds number. This linearity also seems to hold for shear-thickening fluids, but the dependence is seen to be slightly weaker in shear-thinning fluids (Fig. 7) which is in a sense consistent with the aforementioned discussion on the delayed wake formation

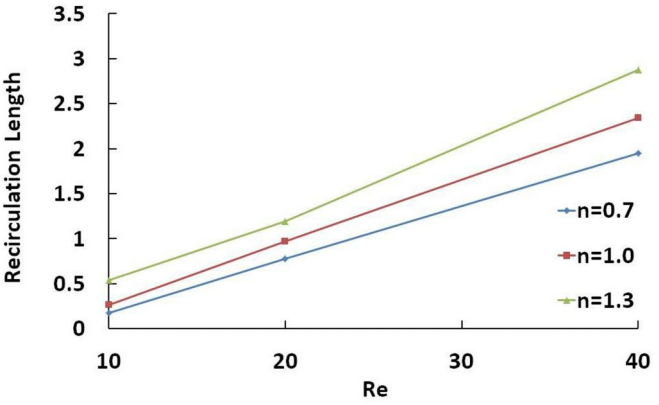

FIG. 7. (Color online) The variation of recirculation length with respect to Reynolds number in different power-law indices.

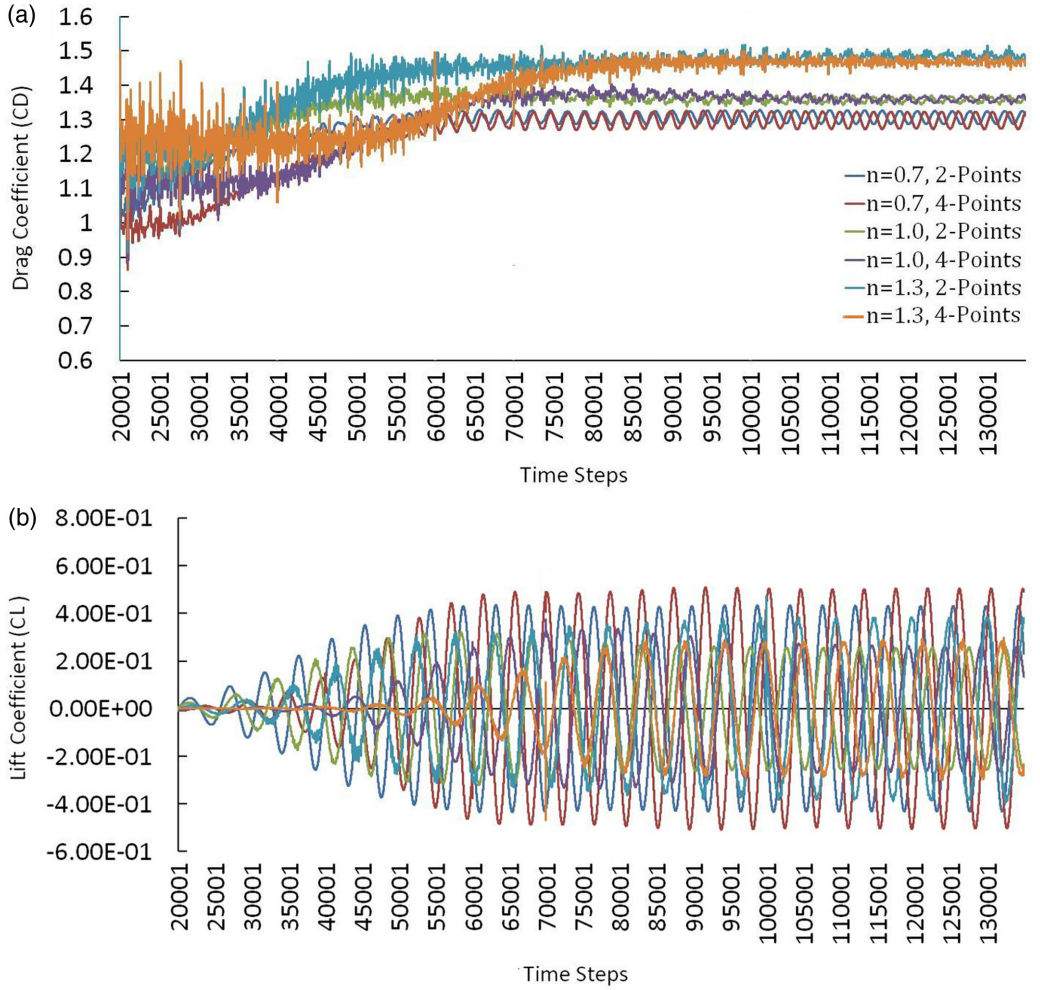

FIG. 8. (Color online) Time evolution of (a) drag and (b) lift coefficients for the shear-thinning ($n = 0.7$), and shear-thickening ($n = 1.3$), non-Newtonian and Newtonian fluids at Re = 100 (NF = 20).

in these systems. Figures 4(c), 5(c), and 6(c) are presented in 135×10^3 time step. As seen from these figures, the place and the size of the vortex which is formed behind the cylinder in the same time is highly dependent on the power-law index.

2. *Time evolution of drag and lift coefficients*

Figures 8(a) and 8(b) represent the time evolution (in 100×10^3 steps) of drag and lift coefficients for the shear-thinning ($n = 0.7$), shear-thickening ($n = 1.3$), non-Newtonian, and Newtonian fluids at Re = 100, respectively. These figures are depicted for both two-point and four-point interface schemes and NF = 20. As seen from these figures, in the unsteady state, the variations of drag and lift coefficients are periodic for both interface schemes. The periodic time increases with the growth of power-law indices for both drag and lift coefficients. Although there is no significant difference for drag coefficient values in two-point and four-point interface schemes, the difference of lift coefficient are considerable for these interface schemes. The lift coefficient values related to the two-point

TABLE VIII. The average Nusselt number for different power-law indices and Reynolds number.

		$n = 0.6$	$n = 0.8$	$n = 1.0$	$n = 1.2$	$n = 1.4$
Re = 20	Two points	3.024107	2.86705	2.788048	2.670105	2.626354
	Four points	3.026998	2.896804	2.791445	2.69953	2.629049
Re = 40	Two points	4.051846	3.869223	3.710647	3.572922	3.467057
	Four points	4.063633	3.869972	3.709672	3.570668	3.461448
		$n = 0.7$	$n = 0.85$	$n = 1.0$	$n = 1.2$	$n = 1.4$
Re = 60	Two points	4.89611	4.68663	4.52172	4.30766	4.14517
	Four points	4.93029	4.64969	4.35909	4.25228	4.09753
Re = 80	Two points	5.73421	5.46021	5.2857	5.02179	4.77764
	Four points	5.72315	5.41414	5.20604	5.00481	4.74103

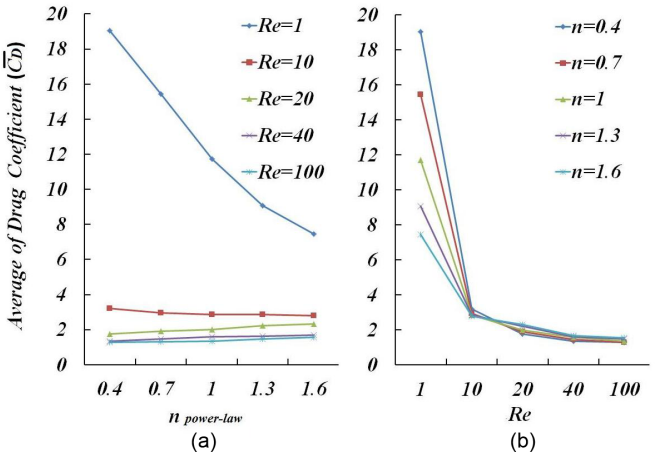

FIG. 9. (Color online) The variation of drag coefficient with respect to (a) the power-law indices at different Reynolds numbers and (b) Reynolds number at different power-law indices.

interface scheme are higher than the corresponding values in the four-point interface scheme for non-Newtonian fluids. In the case of Newtonian fluid, the differences are hardly detectable.

3. The variation of drag coefficient with respect to the Re and n

The variation of drag coefficient with respect to Reynolds numbers (at different power-law indices) and with respect to the power-law indices (at different Reynolds numbers) are shown in Figs. 9(a) and 9(b), respectively. These figures are presented for the two-point interface scheme. According to Fig. 9(a), the drag coefficient generally decreases as the Reynolds number increases for all power-law indices. The slope of variation of the drag coefficient curves is lower for large values of Reynolds numbers [Fig. 9(a)]. As seen from Fig. 9(b), the trend of the drag coefficient with respect to power-law indices is different for low and high Reynolds numbers. At low Reynolds numbers ($\mathrm{Re} < \sim 10$) the skin friction drag is effective. This part of the drag is caused by shear stress on the surface of IB where it is affected by the fluid in which it is immersed. In the low Reynolds number the shear stress on the surface of IB will be decreased with the growth of n and leads to lesser values of drag coefficients. At high Reynolds numbers, in addition to the friction drag, the pressure drag due to the flow separation is important, too. In the high Reynolds numbers ($\mathrm{Re} > \sim 10$), the shedding vortex is larger in higher power-law indices [see Figs. 4(c), 5(c), and 6(c)] which leads to larger amounts of drag coefficient.

4. The variation of average Nusselt number with respect to the Re and n

Table VIII shows the values of average Nusselt number at different Reynolds numbers for both two-point and four-point interface schemes. Table VIII is presented for Newtonian, shear-thinning, and shear-thickening fluids in a wide range of power-law indices at $\mathrm{Pr} = 1$. Implicit direct-forcing ($\mathrm{NF} = 20$) method is used for simulating both momentum and energy equations. Regarding Table VIII, the values of average Nusselt number increase with the growth of Reynolds number in all power-law indices. In the specific value of Reynolds number, the increase of shear-thinning behavior of a non-Newtonian fluid leads to higher values of average Nusselt number, whereas for the shear-thickening behavior an inverse trend will be considered. This phenomenon is related to the lower viscosity of shear-thinning fluids in comparison with the Newtonian and shear-thickening fluids.

VI. CONCLUSIONS

In this paper, the non-Newtonian fluid flow and heat transfer over a cylinder has been investigated using the direct-forcing IB-TLBM. The split-forcing TLBE was used for solving the computational fluid domain. Both two-point and four-point interface schemes are used to compare the effects of boundary sharpness on the accuracy of solution. A simple technique based on predetermined parameters of diffuse IB-TLBM is developed for calculating the Nusselt number. The main results of this study are summarized below:

The IB-TLBM based on split forcing can capture the non-Newtonian behavior of thermal fluid flows in the presence of a heated immersed body in steady or unsteady states.

The on-lattice grid size has a significant effect on the flow characteristics whereas the influence of off-lattice points is not so noteworthy.

In the non-Newtonian steady flows over a cylinder, the shedding vortex length is very sensitive to non-Newtonian behavior indices.

The non-Newtonian behavior index has an important role in the separation phenomenon in unsteady flows of non-Newtonian fluids over an IB.

The drag coefficient reduces with growth of power-law indices in low Reynolds numbers ($\mathrm{Re} < \sim 10$) whereas this variation is inverse for large Reynolds numbers ($\mathrm{Re} > \sim 10$).

The Nusselt number is very sensitive to power-law index in a way that the heat transfer will be increased with the increment of shear-thinning behavior of non-Newtonian fluid.

Since the IB method is highly suitable for simulating moving boundaries, the current in the IB-TLBM algorithm can be considered as a base structure for investigating flow and heat transfer in non-Newtonian fluids with moving bodies in future studies.

[1] R. P. Chhabra and J. F. Richardson, *Non-Newtonian Flow in the Process Industries: Fundamentals and Engineering Applications* (Butterworth-Heinemann, Oxford, 1999).

[2] R. K. Gupta, *Polymer and Composites Rheology*, 2nd ed. (Marcel Dekker, New York, 2000).

[3] R. Clift, J. Grace, and M. E. Weber, *Bubbles, Drops and Particles* (Academic Press, New York, 1978).

[4] M. Coutanceau and J. R. Defaye, Appl. Mech. Rev. **44**, 255 (1991).

[5] C. H. K. Williamson, Annu. Rev. Fluid Mech. **28**, 477 (1996).

[6] M. M. Zdravkovich, *Flow Around Circular Cylinders, Volume 1: Fundamentals* (Oxford University Press, New York, 1997).

[7] M. M. Zdravkovich, *Flow Around Circular Cylinders, Volume 2: Applications* (Oxford University Press, New York, 2003).

[8] C. S. Peskin, Ph.D. thesis, Albert Einstein College of Medicine, 1972.

[9] R. Verzicco, J. Mohd-Yusof, P. Orlandi, and D. Haworth, AIAA J. **38**, 427 (2000).

[10] E. A. Fadlun, R. Verzicco, P. Orlandi, and J. Mohd-Yusof, J. Comput. Phys. **161**, 35 (2000).

[11] C. S. Peskin, J. Comput. Phys. **25**, 220 (1977).

[12] D. Goldstein, R. Handler, and L. Sirovich, J. Comput. Phys. **105**, 354 (1993).

[13] E. M. Saiki and S. Birigen, J. Comput. Phys. **123**, 450 (1996).

[14] M. C. Lai and C. S. Peskin, J. Comput. Phys. **160**, 705 (2000).

[15] Z. G. Feng and E. E. Michaelides, J. Comput. Phys. **195**, 602 (2004).

[16] J. Mohd-Yusof, in CTR Annual Research Briefs, NASA–Stanford University, 1997, p. 317.

[17] J. Kim, D. Kim, and H. Choi, J. Comput. Phys. **171**, 132 (2001).

[18] A. L. F. L. E. Silva, A. Silveira-Neto, and J. J. R. Damasceno, J. Comput. Phys. **189**, 351 (2003).

[19] S. Chen and G. D. Doolen, Annu. Rev. Fluid Mech. **30**, 329 (1998).

[20] D. Yu, M. R. Mei, L. S. Luo, and W. Shyy, Prog. Aerosp. Sci. **39**, 329 (2003).

[21] R. Benzi, S. Succi, and M. Vergassola, Phys. Rep. **222**, 145 (1992).

[22] A. Mussa, P. Asinari, and L. S. Luo, J. Comput. Phys. **228**, 983 (2009).

[23] X. Ku and J. Lin, Mod. Phys. Lett. B. **19**, 1551 (2005).

[24] A. M. Artoli and A. Sequeira, in *Computational Science–ICCS 2006*, Lecture Notes in Computer Science Vol. 3992 (Springer, Berlin, 2006), p. 78.

[25] D. Kehrwald, J. Stat. Phys. **121**, 223 (2005).

[26] S. Gabbanelli, G. Drazer, and J. Koplik, Phys. Rev. E. **72**, 046312 (2005).

[27] J. Boyd, J. M. Buick, and S. Green, J. Phys. A. **39**, 14241 (2006).

[28] E. Aharonov and D. H. Rothman, Geophys. Res. Lett. **20**, 679 (1993).

[29] S. Melchionnaa, M. Bernaschi, S. Succi, E. Kaxiras, F. J. Rybicki, D. Mitsouras, A. U. Coskun, and C. L. Feldman, Comput. Phys. Commun. **181**, 462 (2010).

[30] A. Nejat, V. Abdollahi, and K. Vahidkhah, J. Non-Newtonian Fluid Mech. **166**, 689 (2011).

[31] K. Fallah, M. Khayat, M. H. Borghei, A. Ghaderi, and E. Fattahi, J. Non-Newtonian Fluid Mech. **177-178**, 1 (2012).

[32] G. Pontrelli, S. Ubertini, and S. Succi, J. Stat. Mech.: Theory Exp. (2009) P06005.

[33] O. Malaspinas, G. Courbebaisse, and M. Deville, Int. J. Mod. Phys. C **18**, 1939 (2007).

[34] J. Psihogios, M. E. Kainourgiakis, and A. G. Yiotis, Transp. Porous Media **70**, 279 (2007).

[35] Y. L. Chen, X. D. Cao, and K. Q. Zhu, J. Non-Newtonian Fluid Mech. **159**, 130 (2009).

[36] E. S. Boek, J. Chin, and P. V. Coveney, Int. J. Mod. Phys. B **17**, 99 (2003).

[37] R. Mei, L. S. Luo, and W. Shyy, J. Comput Phys. **155**, 307 (1999).

[38] Z. Guo, C. Zheng, and B. Shi, Phys. Fluids **14**, 2007 (2002).

[39] V. K. Patnana, R. P. Bharti, and R. P. Chhabra, Int. J. Heat Mass Transfer **53**, 4152 (2010).

[40] R. P. Bharti, P. Sivakumar, and R. P. Chhabra, Int. J. Heat Mass Transfer **51**, 1838 (2008).

[41] R. P. Bharti, R. P. Chhabra, and V. Eswaran, Int. J. Heat Mass Transfer **50**, 977 (2007).

[42] A. A. Soares, J. M. Ferreira, and R. P. Chhabra, Ind. Eng. Chem. Res. **44**, 5815 (2005).

[43] S. K. Kang and Y. A. Hassan, Int. J. Numer. Methods Fluids **66**, 1132 (2011).

[44] J. Wu and C. Shu, J. Comput. Phys. **228**, 1963 (2009).

[45] S. K. Kang and Y. A. Hassan, Comput. Fluids **49**, 36 (2011).

[46] J. Wu, C. Shu, and N. Zhao, J. Appl. Math. **2012**, 161484 (2012).

[47] Z. Guo, C. Zheng, and B. Shi, Phys. Rev. E **65**, 046308 (2002).

[48] F. J. H. Gijsen, Ph.D. thesis, Eindhoven University of Technology, 1998.

[49] P. Neofytou and D. Drikakis, J. Non-Newtonian Fluid Mech. **111**, 127 (2003).

[50] M. A. Hussain, S. Kar, and R. R. Puniyani, J. Biosci. **24**, 329 (1999).

[51] P. L. Bhatnagar, E. P. Gross, and M. Krook, Phys. Rev. **94**, 511 (1954).

[52] U. Frisch, D. d'Humières, B. Hasslacher, P. Lallemand, Y. Pomeau, and J.-P. Rivet, Complex Syst. **1**, 649 (1987).

[53] S. Wolfram, J. Stat. Phys. **45**, 471 (1986).

[54] B. Chopard and M. Droz, *Cellular Automata Modeling of Physical Systems* (Cambridge University Press, Cambridge, UK, 1998).

[55] A. Artoli, Ph.D. thesis, University of Amsterdam, 2003.

[56] Z. G. Feng and E. E. Michaelides, J. Comput. Phys. **202**, 20 (2005).

[57] Y. Sui, Y. T. Chew, P. Roy, and H. T. Low, Int. J. Numer. Methods Fluids **53**, 1727 (2007).

[58] A. Dupuis, P. Chatelain, and P. Koumoutsakos, J. Comput. Phys. **227**, 4486 (2008).

[59] C. S. Peskin, Acta Numerica **11**, 479 (2002).

[60] K. Luo, J. Wang, and K. Cen, Phys. Rev. E. **76**, 066709 (2007).

[61] Z. Wang, J. Fan, and K. Luo, Int. J. Multiphase Flow **34**, 283 (2008).

[62] S. W. Su, M. C. Lai, and C. A. Lin, Comput. Fluids **36**, 313 (2007).

[63] D. V. Le, B. C. Khoo, and K. M. Lim, Comput. Methods Appl. Mech. Eng. **197**, 2119 (2008).

[64] C. H. Wang and J. R. Ho, Comput. Math. Appl. **62**, 75 (2011).

[65] J. Park, K. Kwon, and H. Choi, KSME International Journal **12**, 1200 (1998).